AGU ADVANCING EARTH AND SPACE SCIENCES

Geophysical Research Letters

RESEARCH LETTER
10.1029/2024GL113129

Three-Dimensional Characterization of Global Ionospheric Disturbances During the 15 January 2022 Tonga Volcanic Eruption

Changzhi Zhai[1], Shun-Rong Zhang[2], Yibin Yao[3], Wenjun Dong[4,5], Ercha Aa[2], Jian Kong[6], Dongjie Yue[1], Yutian Chen[1], Wenjie Peng[3], and Tingting Yu[7]

[1]School of Earth Sciences and Engineering, Hohai University, Nanjing, China, [2]Haystack Observatory, Massachusetts Institute of Technology, Westford, MA, USA, [3]School of Geodesy and Geomatics, Wuhan University, Wuhan, China, [4]Department of Physical Sciences, Center for Space and Atmospheric Research (CSAR), Embry-Riddle Aeronautical University, Daytona Beach, FL, USA, [5]Global Atmospheric Technologies and Sciences (GATS), Boulder, CO, USA, [6]Chinese Antarctic Center of Surveying and Mapping, Wuhan University, Wuhan, China, [7]Key Laboratory of Earth and Planetary Physics, Institute of Geology and Geophysics, Chinese Academy of Sciences, Beijing, China

Key Points:

- The horizontal speed of the ionospheric disturbances showed a prominent dependence on altitude and azimuth
- The ionospheric disturbances had a much larger vertical wavelength than gravity waves, and their arrival times coincided with Lamb waves
- Lamb waves induced local thermospheric horizontal wave propagation that is faster than their propagation at lower altitudes

Supporting Information:

Supporting Information may be found in the online version of this article.

Correspondence to:

Y. Yao and J. Kong,
ybyao@whu.edu.cn;
jkong@whu.edu.cn

Citation:

Zhai, C., Zhang, S.-R., Yao, Y., Dong, W., Aa, E., Kong, J., et al. (2025). Three-dimensional characterization of global ionospheric disturbances during the 15 January 2022 Tonga volcanic eruption. *Geophysical Research Letters*, *52*, e2024GL113129. https://doi.org/10.1029/2024GL113129

Received 15 OCT 2024
Accepted 16 DEC 2024

Abstract The global 3-dimensional structure of the concentric traveling ionospheric disturbances (CTIDs) triggered by 2022 Tonga volcano was reconstructed by using the 3-dimensional computerized ionospheric tomography (3DCIT) technique and extensive global navigation satellite system (GNSS) observations. This study provides the first estimation of the CTIDs vertical wavelengths, ∼736 km, which was much larger than the gravity wave (GW) vertical wavelength, 240–400 km, estimated using ICON neutral wind observations. Notable trend with the variation of azimuth was also found in horizontal speeds at 200 and 500 km altitudes and differences between them. These results imply that (a) the global propagation of Lamb waves determined the arrival time of local ionospheric disturbances, and (b) the arriving Lamb waves caused vertical atmospheric perturbations that are not typical of GWs, resulting in local thermospheric horizontal wave propagation which is faster than the Lamb wave propagation at lower altitudes.

Plain Language Summary After the 2022 Tonga volcano eruption, atmospheric waves including Lamb waves, gravity waves, acoustic waves were triggered in the lower atmosphere (below 100 km altitude) and the concentric traveling ionospheric disturbances (CTIDs) were also observed above 100 km altitude. However, since these atmospheric waves can have similar horizontal wavelength and speeds, it is challenging to determine the driver of the ionospheric disturbances using 2D GNSS Total Electron Content measurements or satellite in-situ observations. In this study, the GNSS ionospheric tomography technique is employed to reconstruct 3D structures in different regions. The horizontal speeds of CTIDs showed different features at different altitudes and azimuths. In addition, the gravity vertical wavelength estimated using ICON neutral wind observation is much smaller than the tomography derived vertical wavelength. At the same time, most of the CTIDs arrival times coincided with the speed of the Lamb waves.

1. Introduction

During gigantic geological hazards, including huge earthquakes, volcanic eruptions and tsunamis, prominent atmospheric waves can be generated. Due to the near-exponential decrease of the atmospheric density with altitude, the amplitudes of these waves can increase significantly. The waves that propagate upward to the thermospheric altitudes can cause traveling ionospheric disturbances (TIDs) through ion-neutral collisional momentum transfer (Francis, 1973; Huba et al., 2015). The Hunga Tonga–Hunga Ha'apai volcano (hereafter Tonga) at 20.54° S, 175.38° W, erupted at 04:14:45 UT on 15 January 2022 (Wright et al., 2022). It excited prominent waves from the Earth surface to the ionosphere altitudes. Lamb waves with ∼315 m/s phase speed was observed by both surface stations and satellites (Watanabe et al., 2022; Wright et al., 2022). CTIDs were found in New Zealand firstly at about 05:00 UT and reached Australia region at about 06:30 UT (Lin et al., 2022; Themens et al., 2022). Conjugate CTIDs were also observed in the Japan region at about 08:00 UT, which was much earlier than the arrival time of the surface air pressure waves (Lin et al., 2022; Themens et al., 2022). According to the Global Navigation Satellite System (GNSS) Total Electron Content (TEC) observations, TIDs with different speeds and wavelengths also appeared in different regions, and the TIDs with 300–350 m/s traveling speed and

500–1,000 km horizontal wavelength propagated for three times around the Earth (Heki, 2022; Rakesh et al., 2022; Themens et al., 2022).

It should be noted that although the ions follow the neutral wind disturbances along the magnetic field lines, the ion motion across the magnetic field lines is constrained by gyro-motions (Hines, 1968; Hooke, 1968; C. H. Liu & Yeh, 1969). Thus, the configuration of geomagnetic field can cause asymmetric propagation features of the CTIDs in different directions (C. H. Chen et al., 2011; Chou et al., 2017; K. Heki & Ping, 2005). At the same time, the growth of neutral temperature with altitude would allow faster atmospheric wave velocity and may induce faster CTIDs at higher altitudes, assuming atmospheric waves are not significantly damping with increasing height (Beer, 1972; Francis, 1973). Since the atmospheric density decreases with altitude and the ionospheric plasma density varies with altitude, the drag forcing on the ions in ion-neutral coupling would vary with altitude and may also influence the propagation characters of the CTIDs at different altitudes (Ieda, 2020; Tsuda et al., 2007). Thus, the real propagation situation of CTIDs at different altitudes and different azimuths under the influences of these multiple factors is complicated and not fully understood.

Perhaps more significantly, many challenges exist in understanding some fundamental processes responsible for the global responses in the upper atmosphere well above and far away from the epicenter at Tonga. Tonga observations and simulations suggested several candidate drivers of the TIDs global propagation: primary and secondary gravity waves (GWs) (Huba et al., 2023; Vadas et al., 2023) and lamb waves (H. L. Liu et al., 2023; S. Zhang et al., 2022). As mentioned above, extensive studies have been conducted on the eruption induced TIDs. However, most of the previous studies were based on the two-dimensional TEC observations or localized measurements from radars and satellites. More three-dimensional features of the global traveling TIDs remain to be revealed and further studies are needed to explore these various different possible mechanisms.

The present study provides a new approach and new evidence to enable new insights into these scientific challenges. Using GNSS TEC measurements, the 3DCIT technique is capable to reconstruct the three-dimensional ionospheric electron density values (Austen et al., 1988; Seemala et al., 2014; Wen et al., 2011). Taking advantage of the 3DCIT technique and the dense GNSS networks in New Zealand (NZ), Australia (AU), China (CN) and the United States (US), the three-dimensional propagation characteristics of the Tonga volcano induced TIDs with a period between 30 and 50 min are investigated in this study. These new analysis allows to identify likely physical processes involved in the strong whole atmospheric coupling, yielding unprecedented geospace effects.

2. Data and Methodology

TEC data from 182 GNSS ground receivers in NZ, 895 in AU, 253 in CN and 1,221 in US is used in this study. These regions have considerable GNSS data coverages, enabling high-precision 3-D ionospheric reconstruction (Figures S1 and S2 in Supporting Information S1). These regions are used in this study to represent key ionospheric responses as a function of height, distance, and azimuth.

Bandpass filtered slant TECs (dSTECs) with the time period between 30 and 50 min is utilized for the ionospheric electron density reconstruction. The improved constrained simultaneous iterative reconstruction technique (Yao et al., 2020) is used to reconstruct electron density values (Text S1). The four regions mentioned above are selected for 3DCIT reconstruction. Since NZ and AU regions are close, the two regions are reconstructed together. The horizontal resolution is $0.5° \times 0.5°$ in latitude and longitude, and the altitude range extends from 100 to 1,000 km with the vertical resolution of 10 km. There are 8.1×10^5 voxels in the NZ-AU region, and 9.0×10^5 voxels in the CN and US regions. To capture the electron density variations, the time resolution is set to 30 s. The numbers of TEC measurements in the four regions are shown in Figure S3 in Supporting Information S1 and the voxel penetration rates by GNSS rays are provided in Figure S4 in Supporting Information S1.

For validating the reliability of the reconstructed TIDs results, the 3DCIT dSTECs are compared with original bandpass filtered GNSS dSTECs for several selected GNSS receiver-satellite pairs. The 3DCIT dSTECs are integral of reconstructed electron density along GNSS line-of-sight (LOSs). The reconstructed ionospheric fluctuations in 3D showed good agreement with those in the original GNSS dSTEC in NZ, AU, CN and US reconstruction regions (Figure S5 in Supporting Information S1). The proportions of difference values within ±0.2 TECU in NZ-AU, CN and US regions are 76%, 77%, and 85%, respectively. In addition, we compared the 3DCIT results with the available data from the ionosonde MHJ45 station. The electron density time series at

200 km altitude was selected and filtered with a 30–50 min bandpass. To eliminate the effects of bandpass filtering, noise, and the differences between the GNSS and ionosonde detection methods, we normalized the two sets of data to [−1, 1]. As we can see in Figure S7 in Supporting Information S1, the 3DCIT results showed good agreement with ionosonde observations. The results suggest a certain level of reliability in the 3DCIT results.

One of scientific goals of this study is to explore if the volcanic generated waves with 30–50 min periodicities possess any GWs characteristics, thus we examine the GWs dispersion. To simplify our calculation, we assume GWs propagate in the distance and altitude plane, neglecting the variation of horizontal wind with altitude. The dispersion relation for evolving linear, inviscid GWs in a nonrotating and isothermal atmosphere can then be expressed as:

$$m^2 = \frac{N^2}{(c - U_{h0})^2} - k^2 - \frac{1}{4H_S^2}$$
$$N^2(z) = \frac{g(z)}{T_0(z)}\left[\frac{dT_0(z)}{dz} + \frac{g(z)}{C_p}\right] \quad (1)$$

Here N is the buoyancy frequency; k and m are the horizontal and vertical wave numbers, respectively, c is horizontal phase velocity, U_{h0} is background wind, H_S is the scale height, z is altitude, g is the gravitational acceleration and T_0 is neutral temperature, C_P is the specific heat capacity at constant pressure.

Thermospheric neutral wind observations from the ICON satellite (Englert et al., 2017; Makela et al., 2020) and simulations from the thermosphere-ionosphere-electrodynamics general circulation model (TIEGCM) (Qian et al., 2014) are used to estimate the theoretical vertical wavelength of GWs. The model with 2.5° horizontal resolution and 0.25 scale height vertical resolution is driven by realistic interplanetary and solar wind indices.

3. Results

Figure 1 shows the altitudinal (300 km) and azimuthal slices of the 3DCIT electron density results in different regions. CTIDs passed through the NZ region during 05:00−07:20 UT (see Movie S1). At 05:50 UT, two positive and one negative wavefronts were reconstructed in the NZ region, which were approximately parallel to the iso-distance lines (Figure 1a1). Along the 205° azimuth (Figure 1a2), the CTID wavefronts titled outward and upward above ∼100 km at near 2.3 K (where "K" represents 1,000 km) distance from the epicenter and reached ∼800 km altitude at near 3 K distance. In the AU region, the first prominent wavefront of CTIDs appeared at the distance of 4,700 km at ∼08:10 UT and moved westward (see Movie S2). More CTIDs emerged between 3,500 and 6,000 km distance during 08:20−10:20 UT. As we can see in Figures 1b1 and 1b2, the horizontal distribution of CTIDs in AU region were also parallel to iso-distance lines and the vertical distribution was between 100 and 600 km altitude.

CTIDs appeared in the CN region between 10,000 and 11,500 km distance during 12:20-14:10 UT with a magnitude of 0.3×10^{11}el/m^3 (Movie S3). The altitude range of CTIDs in CN region was between 150 and 550 km (Figure 1c2). In US region, TIDs passed through during 13:20−15:20 UT with a magnitude of 0.3×10^{11}el/m^3 (Movie S4). Different from the other three regions, the TID wavefronts in the US region were not always parallel to iso-distance lines (Figure 1d1 and Movie S4), indicating either other sources of TIDs or complicated TID/GW patterns. In particular, the non-concentric phase front nature might be caused also by the anisotropic background neutral wind.

We next investigate the traveling speeds at different altitudes and azimuths. The wavefronts that traveled over 500 km, lasted more than 30 min, and with speeds between 100 and 1,000 m/s are selected. Their propagation speeds were calculated using the time-distance coordinates of their start and end points. Figure 2 shows the azimuthal distribution of CTIDs horizontal speeds at 200 and 500 km altitudes.

The CTIDs speeds at 205° azimuth and 200 km altitude (Figure 2a1, 390–490 m/s) were smaller than that at 500 km (Figure 2a2, 420–690 m/s). However, in AU region, at 235° azimuth, the speeds at 200 km altitude (Figure 2b1) were slightly larger than that at 500 km altitude (Figure 2b2). At 310° azimuth in the CN region which is over 10,000 km distance from the epicenter, the mean speed at 200 km altitude (Figure 2c1, 473 m/s) was

10.1029/2024GL113129

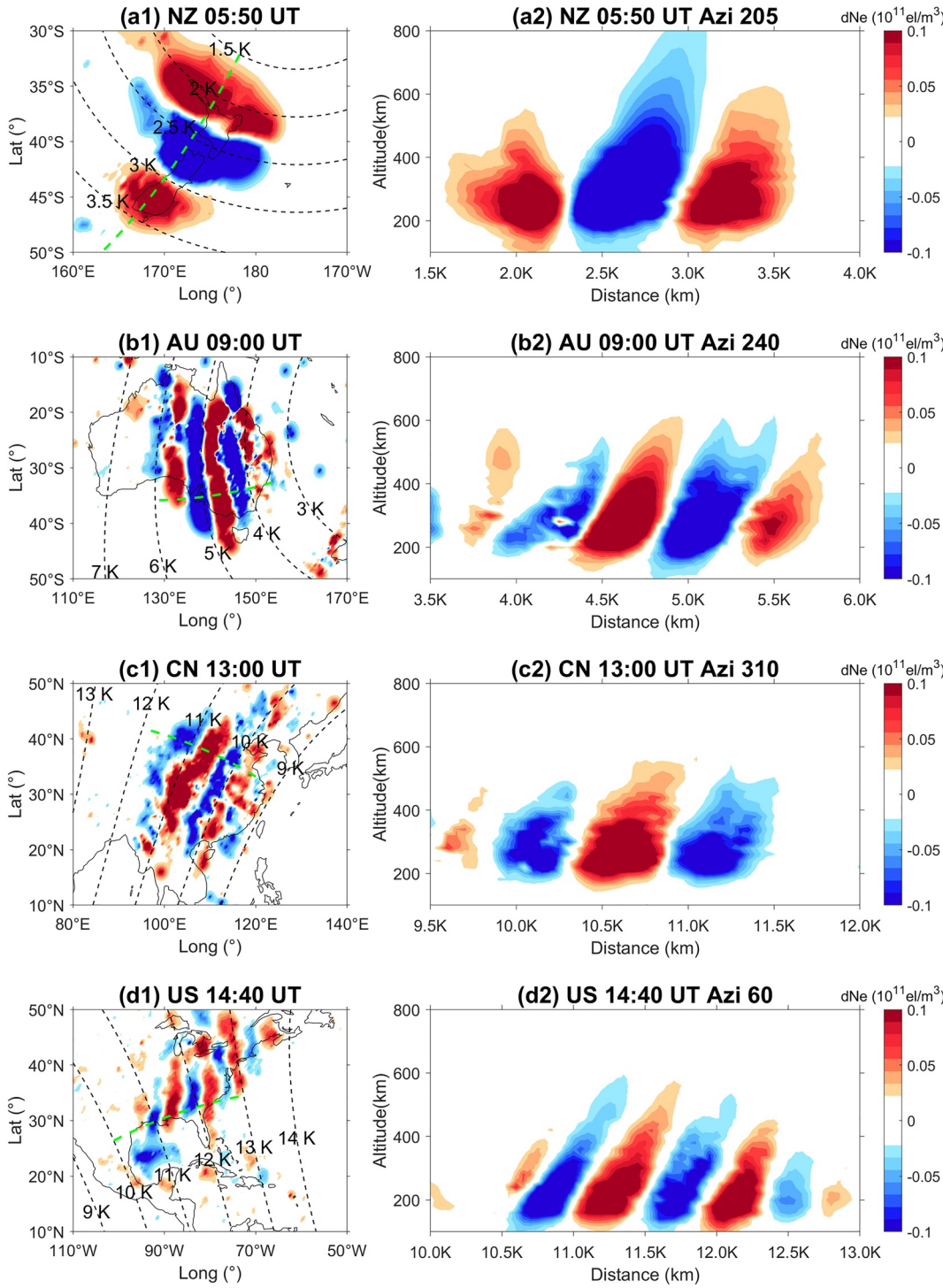

Figure 1. Altitudinal slices at 300 km altitude (left) and azimuthal slices (right) of concentric traveling ionospheric disturbances in NZ, AU, CN, and US regions. The green dashed lines in the left column indicate the position of azimuthal slices of the right column. The iso-distance lines are indicated by black dashed lines. Distances are marked by black texts, "K" represents 1,000 km.

greater than that at 500 km altitude (Figure 2c2, 438 m/s). At azimuth 60° in the US region, similar to azimuths 235° and 310°, the mean speed at 200 km altitude (Figure 2d1, 390 m/s) was greater than that at 500 km (Figure 2d2, 363 m/s).

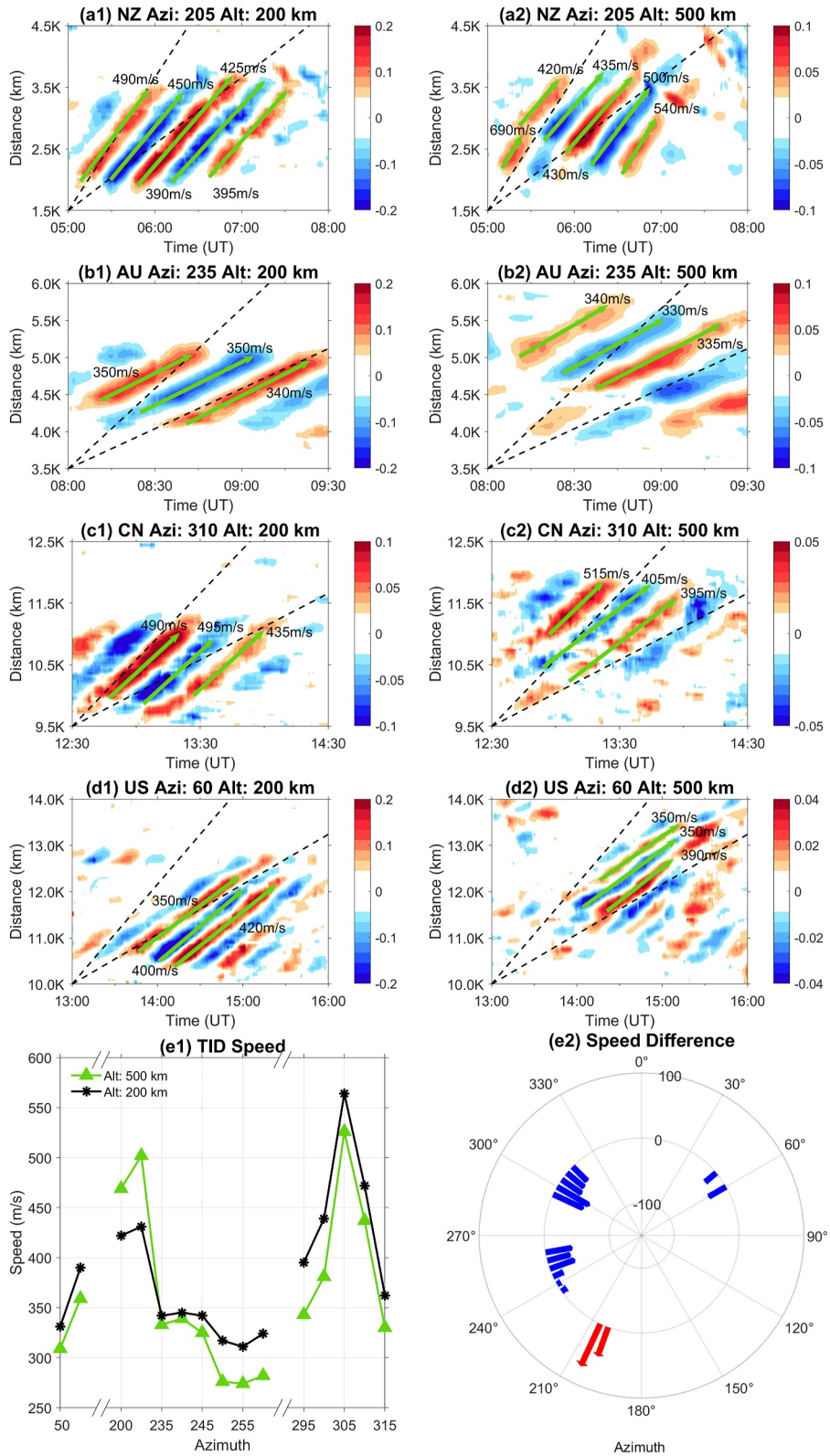

Figure 2. (a–d) Distance-time variation of electron density disturbances at 200 and 500 km altitudes and different azimuths. Prominent wavefronts are indicated by green arrows and horizontal propagation speeds are marked by texts. The slopes of the black dashed lines, arranged clockwise, correspond to 600 m/s and 300 m/s, respectively. (e1) Azimuth distribution of concentric traveling ionospheric disturbances (CTIDs) horizontal propagation speeds at 200 and 500 km altitudes. (e2) Azimuthal distribution of the CTIDs speed difference between 500 and 200 km altitudes (red for positive and blue for negative).

To further investigate the characteristics of CTIDs horizontal propagation speed, more mean values of horizontal speeds at 200 and 500 km altitudes and different azimuths are calculated. Figure 2e1 shows the azimuthal distribution of CITDs horizontal speeds at 200 and 500 km altitudes. The horizontal speed at 200 and 500 km altitudes both increased from 50° to 205°, and decreased from 205° to 255°, and increased again from 255° to 305°. In Figure 2e2, the speed difference between 200 and 500 km altitudes from 200° to 205° increased from +47 to +71 m/s. From 235° to 260°, the speed differences were negative and increased from about −8 to −40. Between 295° and 315°, the difference decreased from about −55 to −30. Conversely, from 50° to 60°, the magnitude of the speed difference increased from −20 to −30. The horizontal speed at 500 and 200 km altitudes and the difference between them both exhibited prominent dependence on azimuth. It is worth noting that the distances between the four regions and the epicenter range from 1.5 to 14 K. The local neutral wind conditions in the near and far-field might also contribute to the speed variations with azimuth (S. Zhang et al., 2022).

Using the 3DCIT results and ICON neutral wind observations, we investigated the features of the vertical propagation of CTIDs, and the relationship between CTIDs and GWs. Figure 3 shows the ICON satellite neutral wind observations (a–f), electron density disturbance profiles at fixed locations in the US region (g) and comparison of vertical wavelengths between 3DCIT and theoretical GWs. More electron density profiles of 3DCIT results with vertical speeds in different regions can be found in Figure S9 in Supporting Information S1.

ICON satellite traversed the south of US during 13:45–14:12 UT and 15:22–15:53 UT on 15 January 2022. Figures 3a and 3b give the tracks of ICON satellite (red dots) during the two time periods, and Figures 3c and 3d show the corresponding altitude-longitude distribution of ICON observed neutral winds, which are projected to the radial direction from Tonga volcano epicenter. For deriving the GW vertical wavelength, the average radial winds between 100 and 300 km altitude are estimated as the background neutral winds. In Figures 3e and 3f, the average radial winds between 100 and 300 km altitude during the two ICON satellite passes were between −75.5 and 14.14 m/s. In Figure 3g, the vertical phase speeds observed in US region ranged from 277 to 333 m/s. Vertical wavelengths were between 664 and 799 km.

The 3DCIT results and ICON neutral wind observations provide a great opportunity for investigating the source of the CTIDs in US region. In Figure 3g, the vertical wavelengths of CTIDs in US region were between 664 and 799 km and the mean value was 736 km. The color plot in Figure 3h shows the theoretical vertical wavelength (λ_Z) and the dispersion curve of 3DCIT λ_Z is indicated by the black dashed line. The feasible theoretical GW λ_Z in US region is derived from GW dispersion relation based on ICON neutral wind observations and TIEGCM simulations. Specifically, in Equation 1, the background neutral wind U_{h0} is set between −75.5 and 14.14 m/s (Figures 3e and 3f). According to the TIEGCM simulations at 200 km altitude, 12,000 km distance from the epicenter with azimuth 60°, the neutral temperature T_0 is between 760 and 850 K (K) from 13:00 to 16:00 UT and the mean value of C_p is 1165.3 J kg^{-1} K^{-1} (Banks & Kockarts, 1973). The horizontal wavelength is 800 km and the buoyancy frequency is calculated using the mean C_p value and TIEGCM simulated temperature data. Thus, the feasible GW λ_Z in US region during 13:45-14:12 UT and 15:22-15:53 UT fall into an area inside the yellow dashed rectangle in Figure 3h. The maximum and minimum GW λ_Z in this area are 400 and 240 km, respectively. There is a significant discrepancy between the theoretical GW and 3DCIT vertical wavelengths in the US region.

4. Discussion

The Tonga volcano eruption induced a broad spectrum of waves which were observed by multi-instruments. However, the observations used in previous studies including TEC, radio occultation and radar observations cannot provide the 3D information of CTIDs such as vertical wavelength, altitudinal range and temporal variations (P. Chen et al., 2023; Lin et al., 2022; Sun et al., 2022; Themens et al., 2022; J. Zhang et al., 2022). In this study, the 3D structure of CTIDs is reconstructed and the vertical wavelength, horizontals speed at different altitude and azimuths are investigated. To analyze the source of these CTIDs, the neutral wind observations from ICON satellite and the neutral temperature from TIEGCM in the US region are used to estimate the vertical wavelength of GWs. In Figure 3h, the theoretical GW vertical wavelength was much smaller than the 3DCIT estimated CTIDs vertical wavelength.

The distance-time variations of electron density at 300 km altitude in the four reconstruction regions are given in Figure 4. Black dashed lines indicate the arrival times of different horizontal speeds, assuming these waves were excited at 04:14:45 UT at Tonga. In the NZ region (Figure 4a), most of the wavefronts arrived between the time

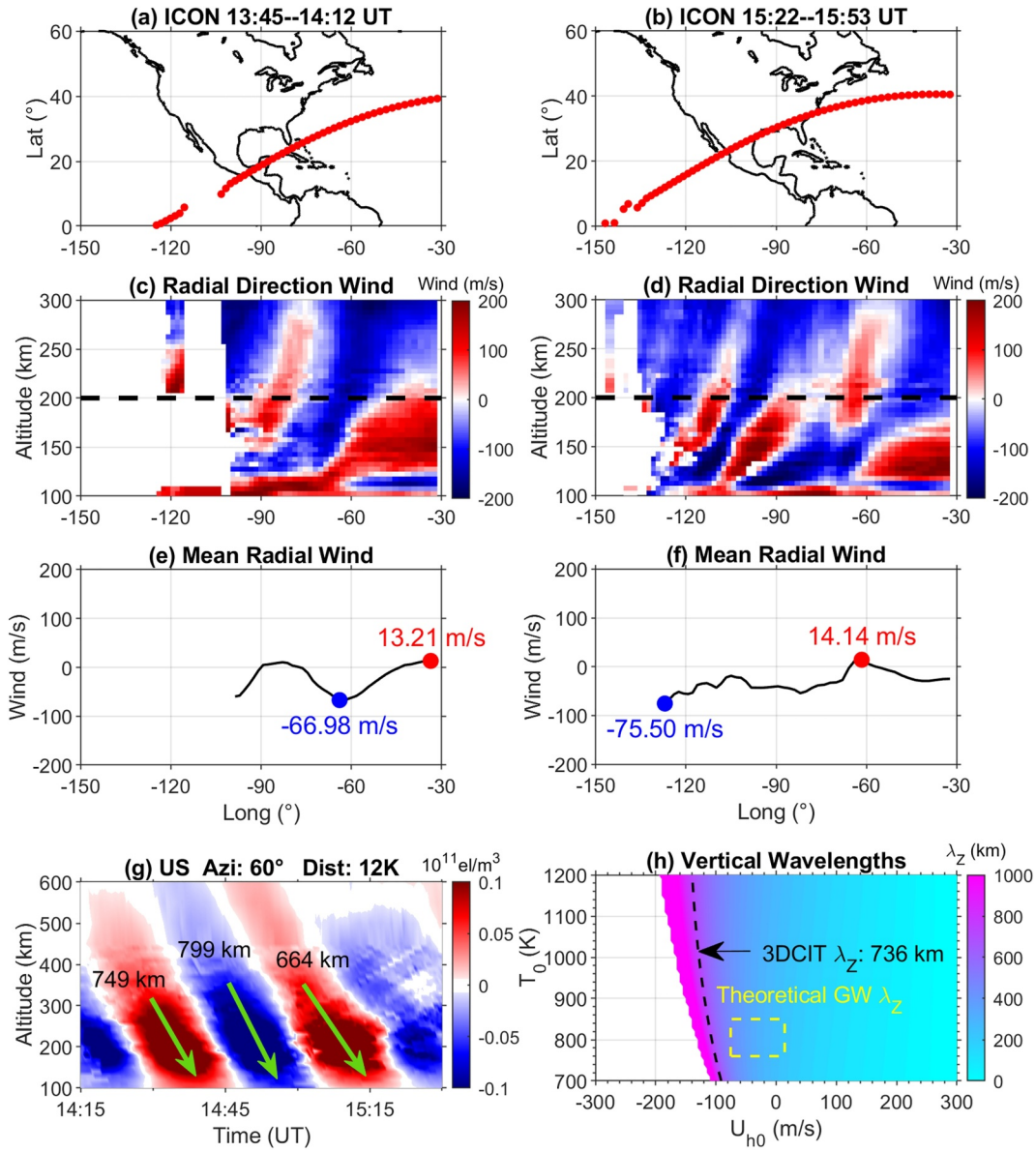

Figure 3. ICON satellite observed neutral wind. (a–b) ICON satellite tracks marked by red dots. (c–d) Altitude-longitude distribution of neutral winds which are projected to the radial direction from the Tonga volcano epicenter (positive outward). (e–f) Average radial neutral wind between 100 and 300 km altitude along the satellite track, their maximum and minimum values are indicated by red and blue texts and dots, respectively. (g) Electron density profiles at fixed locations in US region. (h) Comparison between theoretical gravity wave (GW) vertical wavelength and 3DCIT estimated vertical wavelengths in US region. The dispersion curve of 3DCIT results derived vertical wavelength is indicated by the black dashed line. The feasible theoretical GW vertical wavelengths estimated using ICON neutral wind and TIEGCM neutral temperature are marked by dashed yellow rectangle.

lines of 300 and 600 m/s. In the AU region (Figure 4b), most of the wavefronts arrived between the time lines 250 and 350 m/s. As shown in Figure 4c, the speeds of CTIDs in CN region were between 425 and 530 m/s, while the wavefronts reached 10,500 km distance within the time period between the time lines of 350 m/s and 300 m/s. Similar to the observation in CN region, the wavefronts in US region arrived at the distance of 12,000 km between the time lines of 350 and 300 m/s (Figure 4d). Infrasound, barometer, and volcanic plume observations suggested a complex eruption sequence and major blasts occurred between 04:00-05:00 UT (Matoza et al., 2022; Purkis et al., 2023; Wright et al., 2022). Nevertheless, even assuming that the waves were excited at 05:00 UT, the arrival

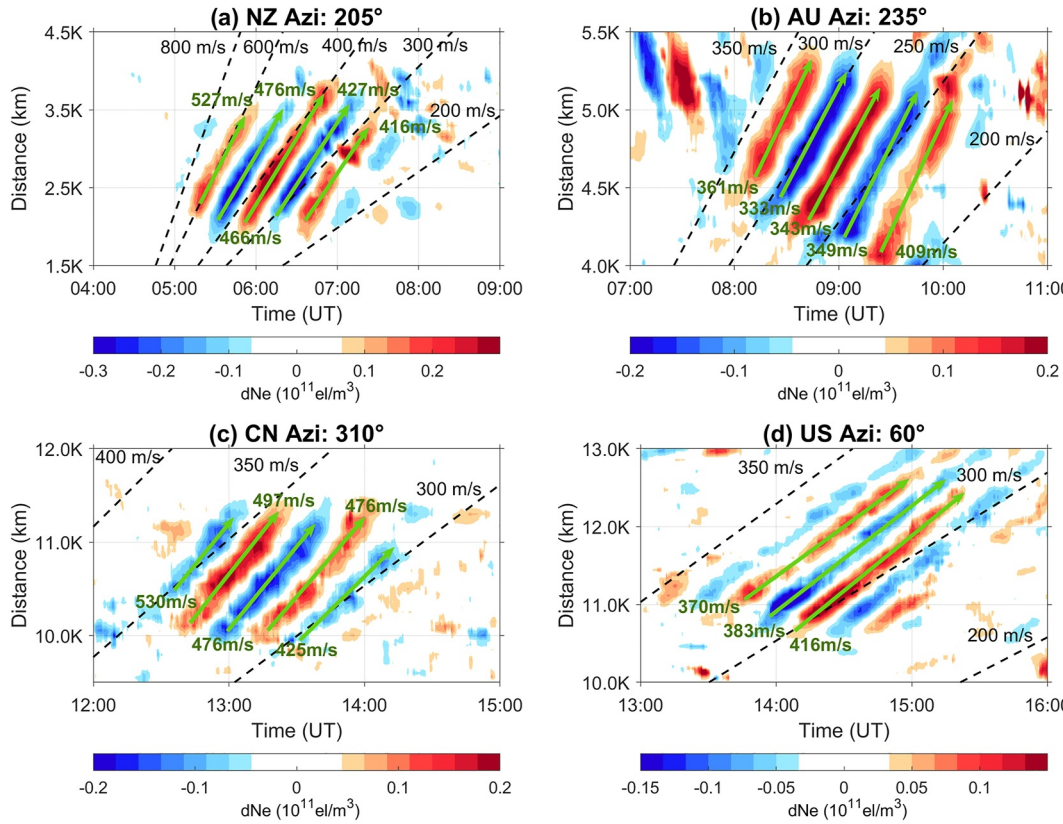

Figure 4. Distance-time variation of electron density disturbances at 300 km altitude in different regions. Prominent wavefronts are highlighted by green arrows, while the corresponding horizontal propagation speeds are indicated with text labels. Black dashed lines indicate the arrival times of different horizontal speeds.

times of CTIDs were still significantly later than the expected arrival times according to their local speeds (Figure S10 in Supporting Information S1).

Therefore, CTIDs in the AU, CN and US regions arrived between the time lines of 250–350 m/s, which coincides with the Lamb wave speeds (Garza-Giron et al., 2023; S. Otsuka, 2022) and would arrive much earlier had they traveled at the local horizontal speeds (330–530 m/s). The simulation results from the Whole Atmosphere Community Climate Model with thermosphere and ionosphere extension (WACCM-X) showed that the Lamb waves propagated at a horizontal phase speed of about 320 m/s in the lower atmosphere (below 100 km altitude). The wavefronts of Lamb waves tilted outward above lower thermosphere and generated ionospheric disturbances (H. L. Liu et al., 2023). The Lamb waves traveled below the thermosphere at a steady speed and their upward propagating wavefronts generated local TIDs above where the majority of Lamb waves energy landed. Thus, the global traveling CTIDs arrival times matched Lamb waves in the lower atmosphere. Due to the increase of the neutral temperature, when the Lamb waves propagated upward into the thermosphere, their horizontal speed increased and the CTIDs exhibited larger local horizontal speed than that of Lamb waves at lower atmosphere.

Though the azimuthal characterization of the TIDs propagation have been analyzed during MSTIDs (Chou et al., 2018; Y. Otsuka et al., 2004; Tsugawa et al., 2007; Zettergren & Snively, 2015; Zhao et al., 2020) or earthquake events(K. Heki & Ping, 2005; J.-Y. Liu et al., 2011; Y. Otsuka et al., 2006; Tsugawa et al., 2011), the results were based on numerical simulations or 2D observations within limited regions and azimuths. The Tonga volcano generated global propagation of CTIDs and the 3DCIT technique provides a great opportunity to investigate the coupling between the thermosphere and ionosphere in a wide azimuth range and three-dimensional scope. Unlike the wave magnitude asymmetries reported in previous studies, the horizontal speeds at 200 and 500 km altitudes exhibited a clear azimuthal dependence (Figures 2e1 and 2e2). The distance and local effects on the horizontal speed might be responsible for the horizontal speed asymmetry. In the NZ region (1.5–3.5 K), a few CTIDs wavefronts arrived earlier than 400 m/s time line and several wavefronts arrived later than 300 m/s time

line (Figure 4a). The vertical speeds in the NZ region were between ~560 and ~800 m/s, which were significantly larger than those in other three regions. The CTIDs in the near field might be caused by hybrid waves, including Lamb, acoustic and GWs (L. Liu et al., 2023; Themens et al., 2022; S. Zhang et al., 2022) and the fast wave components could contribute to the large horizontal speed at 200° and 205° azimuths. Local neutral wind in CN region might be in favor of the propagation of the Lamb waves in thermosphere and caused larger CTIDs horizontal speeds.

5. Conclusion

In this study, we reconstructed the three-dimensional structures and evolutions of the Tonga volcanic eruption excited global CTIDs using the 3DCIT technique. The speeds of CTIDs at altitudes of 200 and 500 km, as well as the difference between them, were calculated, revealing a significant dependence on both altitude and magnetic azimuth. The vertical wavelengths of CTIDs estimated from 3DCIT results were much larger than those of GW. The CTIDs arrival times in different regions were later than expected based on their local speeds but matched those of Lamb waves. Therefore, the globally traveling CTIDs are unlikely caused by GW and are more closely associated with Lamb waves.

Data Availability Statement

The data on which this article is based are available in C. Zhai (2024).

Acknowledgments
This study is supported by National Key Research and Development Program of China (2021YFC3000504), National Natural Science Foundation of China (42104009), Fundamental Research Funds for the Central Universities (B230201012), China Postdoctoral Science Foundation (2022M720988), NSF (AGS-2327914, AGS-1759471). Work at MIT is funded through US NSF Grants AGS-1952737, AGS-2033787, and AGS-2149698, and US ONR Grants N00014-23-1-2160 and N00014-24-1-2122.

References

Austen, J. R., Franke, S. J., & Liu, C. H. (1988). Ionospheric imaging using computerized tomography. *Radio Science*, *23*(3), 299–307. https://doi.org/10.1029/RS023i003p00299

Banks, P. M., & Kockarts, G. (1973). *Aeronomy*. Elsevier.

Beer, T. (1972). Atmospheric waves and the ionosphere. *Contemporary Physics*, *13*(3), 247–271. https://doi.org/10.1080/00107517208205680

Chen, C. H., Saito, A., Lin, C. H., Liu, J. Y., Tsai, H. F., Tsugawa, T., et al. (2011). Long-distance propagation of ionospheric disturbance generated by the 2011 off the Pacific coast of Tohoku Earthquake. *Earth, Planets and Space*, *63*(7), 881–884. https://doi.org/10.5047/eps.2011.06.026

Chen, P., Xiong, M., Wang, R., Yao, Y., Tang, F., Chen, H., & Qiu, L. (2023). On the ionospheric disturbances in New Zealand and Australia following the eruption of the Hunga Tonga-Hunga Ha'apai volcano on 15 January 2022. *Space Weather*, *21*(4), e2022SW003294. https://doi.org/10.1029/2022sw003294

Chou, M. Y., Lin, C. C. H., Huba, J. D., Lien, C. P., Chen, C. H., Yue, J., et al. (2018). Numerical modeling of the concentric gravity wave seeding of low-latitude nighttime medium-scale traveling ionospheric disturbances. *Geophysical Research Letters*, *45*(13), 6390–6399. https://doi.org/10.1029/2018gl077959

Chou, M. Y., Lin, C. C. H., Yue, J., Chang, L. C., Tsai, H. F., & Chen, C. H. (2017). Medium-scale traveling ionospheric disturbances triggered by Super Typhoon Nepartak (2016). *Geophysical Research Letters*, *44*(15), 7569–7577. https://doi.org/10.1002/2017gl073961

Englert, C. R., Harlander, J. M., Brown, C. M., Marr, K. D., Miller, I. J., Stump, J. E., et al. (2017). Michelson interferometer for global high-resolution thermospheric imaging (MIGHTI): Instrument design and calibration. *Space Science Reviews*, *212*(1–2), 553–584. https://doi.org/10.1007/s11214-017-0358-4

Francis, S. H. (1973). Acoustic-gravity modes and large-scale traveling ionospheric disturbances of a realistic, dissipative atmosphere. *Journal of Geophysical Research*, *78*(13), 2278–2301. https://doi.org/10.1029/JA078i013p02278

Garza-Giron, R., Lay, T., Pollitz, F., Kanamori, H., & Rivera, L. (2023). Solid Earth-atmosphere interaction forces during the 15 January 2022 Tonga eruption. *Science Advances*, *9*(2), eadd4931. https://doi.org/10.1126/sciadv.add4931

Heki, K. (2022). Ionospheric signatures of repeated passages of atmospheric waves by the 2022 Jan. 15 Hunga Tonga-Hunga Ha'apai eruption detected by QZSS-TEC observations in Japan. *Earth, Planets and Space*, *74*(1), 112. https://doi.org/10.1186/s40623-022-01674-7

Heki, K., & Ping, J. (2005). Directivity and apparent velocity of the coseismic ionospheric disturbances observed with a dense GPS array. *Earth and Planetary Science Letters*, *236*(3–4), 845–855. https://doi.org/10.1016/j.epsl.2005.06.010

Hines, C. O. (1968). An effect of ohmic losses in upper atmospheric gravity waves. *Journal of Atmospheric and Terrestrial Physics*, *30*(5), 851–856. https://doi.org/10.1016/s0021-9169(68)80037-6

Hooke, W. H. (1968). Ionospheric irregularities produced by internal atmospheric gravity waves. *Journal of Atmospheric and Terrestrial Physics*, *30*(5), 795–823. https://doi.org/10.1016/S0021-9169(68)80033-9

Huba, J. D., Becker, E., & Vadas, S. L. (2023). Simulation study of the 15 January 2022 Tonga event: Development of super equatorial plasma bubbles. *Geophysical Research Letters*, *50*(1), e2022GL101185. https://doi.org/10.1029/2022gl101185

Huba, J. D., Drob, D. P., Wu, T. W., & Makela, J. J. (2015). Modeling the ionospheric impact of tsunami-driven gravity waves with SAMI3: Conjugate effects. *Geophysical Research Letters*, *42*(14), 5719–5726. https://doi.org/10.1002/2015gl064871

Ieda, A. (2020). Ion-neutral collision frequencies for calculating ionospheric conductivity. *Journal of Geophysical Research: Space Physics*, *125*(2), e2019JA027128. https://doi.org/10.1029/2019ja027128

Lin, J. T., Rajesh, P. K., Lin, C. C. H., Chou, M. Y., Liu, J. Y., Yue, J., et al. (2022). Rapid conjugate appearance of the giant ionospheric Lamb wave signatures in the Northern Hemisphere after Hunga-Tonga volcano eruptions. *Geophysical Research Letters*, *49*(8), e2022GL098222. https://doi.org/10.1029/2022gl098222

Liu, C. H., & Yeh, K. C. (1969). Effect of ion drag on propagation of acoustic-gravity waves in the atmospheric F region. *Journal of Geophysical Research*, *74*(9), 2248–2255. https://doi.org/10.1029/JA074i009p02248

Liu, H. L., Wang, W., Huba, J. D., Lauritzen, P. H., & Vitt, F. (2023). Atmospheric and ionospheric responses to Hunga-Tonga volcano eruption simulated by WACCM-X. *Geophysical Research Letters*, *50*(10), e2023GL103682. https://doi.org/10.1029/2023gl103682

Liu, J.-Y., Chen, C.-H., Lin, C.-H., Tsai, H.-F., Chen, C.-H., & Kamogawa, M. (2011). Ionospheric disturbances triggered by the 11 March 2011 M9.0 Tohoku earthquake. *Journal of Geophysical Research*, *116*(A6), A06319. https://doi.org/10.1029/2011ja016761

Liu, L., Morton, Y. J., Cheng, P. H., Amores, A., Wright, C. J., & Hoffmann, L. (2023). Concentric traveling ionospheric disturbances (CTIDs) triggered by the 2022 Tonga volcanic eruption. *Journal of Geophysical Research: Space Physics*, *128*(2), e2022JA030656. https://doi.org/10.1029/2022ja030656

Makela, J. J., Baughman, M., Navarro, L. A., Harding, B. J., Englert, C. R., Harlander, J. M., et al. (2020). Validation of ICON-MIGHTI thermospheric wind observations: 1. Nighttime red-line ground-based Fabry-Perot interferometers. *Journal of Geophysical Research: Space Physics*, *126*(2), e2020JA028726. https://doi.org/10.1029/2020ja028726

Matoza, R. S., Fee, D., Assink, J. D., Iezzi, A. M., Green, D. N., Kim, K., et al. (2022). Atmospheric waves and global seismoacoustic observations of the January 2022 Hunga eruption, Tonga. *Science*, *377*(6601), 95–100. https://doi.org/10.1126/science.abo7063

Otsuka, S. (2022). Visualizing Lamb waves from a volcanic eruption using meteorological satellite Himawari-8. *Geophysical Research Letters*, *49*(8), e2022GL098324. https://doi.org/10.1029/2022gl098324

Otsuka, Y., Kotake, N., Tsugawa, T., Shiokawa, K., Ogawa, T., Effendy, et al. (2006). GPS detection of total electron content variations over Indonesia and Thailand following the 26 December 2004 earthquake. *Earth, Planets and Space*, *58*(2), 159–165. https://doi.org/10.1186/bf03353373

Otsuka, Y., Shiokawa, K., Ogawa, T., & Wilkinson, P. (2004). Geomagnetic conjugate observations of medium-scale traveling ionospheric disturbances at midlatitude using all-sky airglow imagers. *Geophysical Research Letters*, *31*(15), L15803. https://doi.org/10.1029/2004gl020262

Purkis, S. J., Ward, S. N., Fitzpatrick, N. M., Garvin, J. B., Slayback, D., Cronin, S. J., et al. (2023). The 2022 Hunga-Tonga megatsunami: Near-field simulation of a once-in-a-century event. *Science Advances*, *9*(15), eadf5493. https://doi.org/10.1126/sciadv.adf5493

Qian, L., Burns, A. G., Emery, B. A., Foster, B., Lu, G., Maute, A., et al. (2014). The NCAR TIE-GCM: A community model of the coupled thermosphere/ionosphere system. In *Modeling the Ionosphere–Thermosphere System* (pp. 73–83).

Rakesh, V., Haridas, S., Sivan, C., Manoj, M. G., Abhilash, S., Paul, B., et al. (2022). Impact of the Hunga Tonga-Hunga Ha'apai volcanic eruption on the changes observed over the Indian near-equatorial ionosphere. *Advances in Space Research*, *70*(8), 2480–2493. https://doi.org/10.1016/j.asr.2022.07.004

Seemala, G. K., Yamamoto, M., Saito, A., & Chen, C.-H. (2014). Three-dimensional GPS ionospheric tomography over Japan using constrained least squares. *Journal of Geophysical Research: Space Physics*, *119*(4), 3044–3052. https://doi.org/10.1002/2013ja019582

Sun, Y.-Y., Chen, C.-H., & Lin, C.-Y. (2022). Detection of vertical changes in the ionospheric electron density structures by the radio occultation technique onboard the FORMOSAT-7/COSMIC2 mission over the eruption of the Tonga underwater volcano on 15 January 2022. *Remote Sensing*, *14*(17), 4266. https://doi.org/10.3390/rs14174266

Themens, D. R., Watson, C., Žagar, N., Vasylkevych, S., Elvidge, S., McCaffrey, A., et al. (2022). Global propagation of ionospheric disturbances associated with the 2022 Tonga volcanic eruption. *Geophysical Research Letters*, *49*(7), e2022GL098158. https://doi.org/10.1029/2022gl098158

Tsuda, T. T., Nozawa, S., Brekke, A., Ogawa, Y., Motoba, T., Roble, R., & Fujii, R. (2007). An ion drag contribution to the lower thermospheric wind in the summer polar region. *Journal of Geophysical Research*, *112*(A6), A06319. https://doi.org/10.1029/2006ja011785

Tsugawa, T., Otsuka, Y., Coster, A. J., & Saito, A. (2007). Medium-scale traveling ionospheric disturbances detected with dense and wide TEC maps over North America. *Geophysical Research Letters*, *34*(22), L22101. https://doi.org/10.1029/2007gl031663

Tsugawa, T., Saito, A., Otsuka, Y., Nishioka, M., Maruyama, T., Kato, H., et al. (2011). Ionospheric disturbances detected by GPS total electron content observation after the 2011 off the Pacific coast of Tohoku Earthquake. *Earth, Planets and Space*, *63*(7), 875–879. https://doi.org/10.5047/eps.2011.06.035

Vadas, S. L., Figueiredo, C., Becker, E., Huba, J. D., Themens, D. R., Hindley, N. P., et al. (2023). Traveling ionospheric disturbances induced by the secondary gravity waves from the Tonga eruption on 15 January 2022: Modeling with MESORAC-HIAMCM-SAMI3 and comparison with GPS/TEC and ionosonde data. *Journal of Geophysical Research: Space Physics*, *128*(6), e2023JA031408. https://doi.org/10.1029/2023ja031408

Watanabe, S., Hamilton, K., Sakazaki, T., & Nakano, M. (2022). First detection of the Pekeris internal global atmospheric resonance: Evidence from the 2022 Tonga eruption and from global reanalysis data. *Journal of the Atmospheric Sciences*, *79*(11), 3027–3043. https://doi.org/10.1175/jas-d-22-0078.1

Wen, D., Wang, Y., & Norman, R. (2011). A new two-step algorithm for ionospheric tomography solution. *GPS Solutions*, *16*(1), 89–94. https://doi.org/10.1007/s10291-011-0211-2

Wright, C. J., Hindley, N. P., Alexander, M. J., Barlow, M., Hoffmann, L., Mitchell, C. N., et al. (2022). Surface-to-space atmospheric waves from Hunga Tonga-Hunga Ha'apai eruption. *Nature*, *609*(7928), 741–746. https://doi.org/10.1038/s41586-022-05012-5

Yao, Y., Zhai, C., Kong, J., Zhao, C., Luo, Y., & Liu, L. (2020). An improved constrained simultaneous iterative reconstruction technique for ionospheric tomography. *GPS Solutions*, *24*(3), 68. https://doi.org/10.1007/s10291-020-00981-4

Zettergren, M. D., & Snively, J. B. (2015). Ionospheric response to infrasonic-acoustic waves generated by natural hazard events. *Journal of Geophysical Research: Space Physics*, *120*(9), 8002–8024. https://doi.org/10.1002/2015ja021116

Zhai, C. (2024). Three-dimensional characterization of global ionospheric disturbances during the 15 January 2022 Tonga volcanic eruption [Dataset]. *Zenodo*. https://doi.org/10.5281/zenodo.10596161

Zhang, J., Xu, J., Wang, W., Wang, G., Ruohoniemi, J. M., Shinbori, A., et al. (2022). Oscillations of the ionosphere caused by the 2022 Tonga volcanic eruption observed with SuperDARN radars. *Geophysical Research Letters*, *49*(20), e2022GL100555. https://doi.org/10.1029/2022gl100555

Zhang, S., Vierinen, J., Aa, E., Goncharenko, L. P., Erickson, P. J., Rideout, W., et al. (2022). 2022 Tonga volcanic eruption induced global propagation of ionospheric disturbances via Lamb waves. *Frontiers in Astronomy and Space Sciences*, *9*, 871275. https://doi.org/10.3389/fspas.2022.871275

Zhao, Y., Deng, Y., Wang, J. S., Zhang, S. R., & Lin, C. Y. (2020). Tropical cyclone-induced gravity wave perturbations in the upper atmosphere: GITM-R simulations. *Journal of Geophysical Research: Space Physics*, *125*(7), e2019JA027675. https://doi.org/10.1029/2019ja027675